ARTICLE

Direct measurement of radiative decay rates in metal halide perovskites

Angelica Simbula,[a] Riccardo Pau,[a,b] Fang Liu,[a] Luyan Wu,[a] Stefano Lai,[a] Alessandra Geddo-Lehmann,[a] Alessio Filippetti,[a,c] Maria A. Loi,[b] Daniela Marongiu,[a] Francesco Quochi,[a] Michele Saba,*[a] Andrea Mura[a] and Giovanni Bongiovanni*[a]

Received 00th January 20xx,
Accepted 00th January 20xx

DOI: 10.1039/x0xx00000x

The rate of light emission per unit carrier concentration, or radiative rate, is a fundamental semiconductor parameter that determines the limit photoconversion efficiency of solar cells. In hybrid perovskites, a champion materials class for photovoltaics, optical emission results from a bimolecular process, so that the radiative rate depends on the carrier density and cannot be directly measured with standard techniques. Instead, it is estimated either from UV-Vis absorption or from the kinetics of photoexcitation decays in time-resolved spectroscopy experiments. In this work, an ultrafast radiometric experiment is introduced to directly assess the radiative decay rate in perovskites thin films through a calibrated measurement of the instantaneous photoluminescence flux under pulsed laser excitation. The measured radiative decay rate is found to be significantly lower than the second order decay constant determined from photoluminescence decay kinetics, contrary to what often assumed; it is also 50-100 times slower than estimates for a plasma of free excitons and free charged carriers, obtained from absorption coefficients through optical reciprocity relations. We attribute the microscopic origin of the measured low radiative rate to the formation of a population of dark excitations, specifically large polarons. Our results provide a coherent framework to rationalize radiative and non-radiative carrier recombination processes in metal halide perovskites, as well as the photophysical basis to optimize device performances for this emerging class of semiconductors.

Introduction

Performances of semiconductor-based optoelectronic devices depend critically on their radiative emission efficiency. While the connection is apparent for light-emitting devices, it holds for solar cells as well, since pure radiative recombination is needed to approach the Shockley-Queisser limit for photoconversion efficiency.[1–4] The goal in solar cell optimization is to reduce unwanted, non-radiative decay rates below the benchmark set by the radiative rate, so that their effects on solar cell efficiency are negligeable. The progress towards the radiative limit has been rapid in solar cells based on hybrid lead-halide perovskites, where in a few years voltage losses due to non-radiative decay have been reduced to the level of the best silicon solar cells.[5–7] However, the actual values of radiative decay rates in perovskites are currently not agreed upon. The catch with perovskite solar cells is that radiative recombination is a bimolecular process whose rate increases proportionally to the carrier concentration. In turn, carrier concentration under continuous-wave (CW) excitation is determined by the balance between generation and recombination rates, so that a CW measurement alone cannot access the radiative recombination rate because carrier concentration is unknown. To supplement CW measurements, ultrafast time-resolved photoluminescence (TRPL) is typically employed to measure real time decay rates for photoexcitations created by ultrafast laser pulses; radiative and non-radiative decay rates are then estimated by fitting the photoluminescence time traces with a rate equation model, also known as the ABC model, that includes a monomolecular term (A), usually attributed to traps, a bimolecular term (B), assumed as radiative recombination, and a trimolecular term (C), due to Auger recombination.[8–11] Such time-domain determination of radiative recombination rates is however based on the unproven assumption that, since radiative recombination is a bimolecular recombination process between two free carriers, then all bimolecular recombination in perovskites is radiative, even though some studies have suggested otherwise.[12–16] Restricting the field to methylammonium lead halide $CH_3NH_3PbI_3$ (MAPI), the prototype of perovskites successfully employed in solar cells, analyses based on rate equations produced a wide variety of results for the bimolecular radiative recombination rate coefficients, within the range $2 \times 10^{-11} \div 2 \times 10^{-8} \mathrm{cm^3 s^{-1}}$.[17–25] Such a wide spread cannot be attributed to variations in the oscillator strength of optical transitions, given that measurements for the absorption coefficient at the exciton peak, which results from the inverse process of optical

[a] Dipartimento di Fisica, Università di Cagliari, Cittadella Universitaria, I-09042 Monserrato (CA), Italy.
E-mail saba@unica.it; giovanni.bongiovanni@dsf.unica.it
[b] University of Groningen, Zernike Institute for Advanced Materials, University of Groningen, Nijenborgh 4, 09747 AG Groningen, The Netherlands.
[c] Istituto Officina dei Materiali (CNR - IOM) Cagliari, Cittadella Universitaria, I-09042 Monserrato (CA), Italy

† Electronic Supplementary Information (ESI) available: See DOI: 10.1039/x0xx00000x

emission,[26,27] are for MAPI consistently reported within a much narrower interval, around $3 \times 10^4 \mathrm{cm}^{-1}$.[21,27–32] This inconsistency has been tentatively attributed to either extrinsic effects, like spatial diffusion and vertical inhomogeneity of charge carriers,[19,20,33,34] or to intrinsic effects that breach the symmetry between absorption and emission, like Rashba effect or the formation of large polarons.[13,35–41] It appears therefore of paramount importance to establish a reliable value for the radiative recombination rate.

The aim of this work is to provide an experimental technique to directly access the radiative recombination rate by measuring at the same time the absolute photon emission flux and the carrier density. In the setup proposed here, ultrafast laser excitation creates a known density of photoexcitations, while the instantaneous absolute flux of photons emitted per unit time is measured with a radiometrically calibrated streak camera set-up. The technique has been applied to a variety of hybrid perovskite compounds of interest for optoelectronics, both with iodine and bromine as halide anions. The values obtained for the radiative recombination rates are at least one order of magnitude lower than the bimolecular decay rates measured from photoluminescence time traces, and up to two orders of magnitude lower than the radiative rates estimated from optical absorption under the assumption of a population of free electrons, holes, and excitons. Such results are interpreted as evidence for the presence of dark photoexcitations, namely the formation of large polarons.

Results

Direct measurement of the radiative decay rates

Direct measurement of the radiative bimolecular recombination constant requires absolute measurements of both the carrier density n and the emitted radiance. When a semiconductor thin film is optically excited above the gap with laser pulses much shorter than the carrier recombination time, the optically injected carrier density, $n(t=0)=n_0$, can be estimated accurately from the pulse photon fluence times the absorptance, divided by the film thickness. The ensuing instantaneous photoluminescence (PL) emitted over a time interval much shorter than the carrier lifetime, namely $PL(t=0)=PL_0$, represents the external light radiance emitted perpendicularly to the films surface, produced by the carrier density n_0. The goal of our experiment is to measure the absolute PL_0 value through a calibrated streak camera spectrometer. A sketch of the experimental setup used for the determination of absolute PL emission is shown in the upper panel of Fig. 1. Optical excitation was provided by a wavelength-tuneable regenerative amplifier laser source delivering 100-fs long pulses at 1KHz repetition rate. A portion of photoluminescence emitted perpendicularly to the sample surface in the backward direction, collected over a small solid angle, is focused onto the entrance slit of a spectrometer coupled to a 2D streak camera. The image of the excitation spot is shown in the left inset of Fig. 1(a), where the small green rectangle, much smaller than the laser spot, represents the

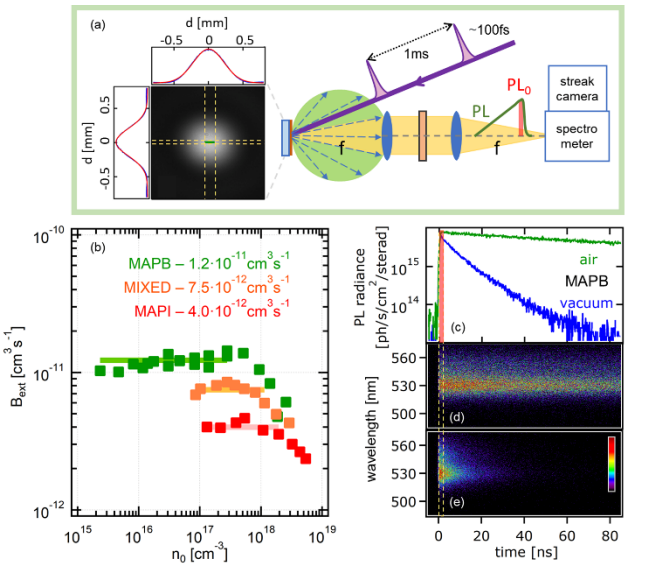

Fig. 1: (a) Sketch of the experimental setup for the measurement of the absolute time resolved PL radiance, with a pulsed source exciting the front side of the sample and a portion (in yellow) of the PL emission being collected and focused on the entrance slit of the time-resolving detection system. Light emission is assumed to follow a Lambertian angular dispersion as represented by the green lobe in front of the sample surface. Inset on the left is an image of the excitation spot in the plane of the sample, with horizontal and vertical profiles fitted by gaussian functions. Here the small homogeneously pumped region probed in the measurement is represented by the green rectangle resulting from the intersection of the images of the spectrometer and streak camera entrance slits. In order to ensure vertically-homogeneous excitation, the pump laser wavelength was 630 nm for MAPI and mixed perovskite films, 430 nm for MAPB. Graph (b): values of B_{ext} obtained from absolute $t=0$ radiance (PL_0) as a function of the injected carried density n_0 for MAPB (green), mixed perovskite (orange), and MAPI (red), with thick lines representing the best fit with a linear function and resulting in the average values reported on top of the graph, excluding the data at high injected carrier density, where Auger effect becomes dominant. PL measurements in the lower carrier density regime for MAPI and MIXED were not accessible due to lower emission efficiency of the samples. On the right side: (c) absolute PL radiance time profiles obtained from spectrograms (d) and (e) measured in the same MAPB sample inside a vacuum chamber, with (d) recorded at atmospheric pressure, and (e) measured at low pressure, temporarily recovering the behaviour previous to photohealing. The two decay profiles in (c) have the same PL_0 but very different photoluminescence decay times.

intersection of the spectrometer vertical entrance slit with the horizontal streak camera slit, highlighting that the probed PL comes from a homogeneously excited region on the in-plane sample surface. The streak camera response was calibrated by directing a laser pulse of known fluence through the same setup through which PL is collected, yielding the detection quantum yield as the ratio between streak camera counts to incident photons; the absolute calibration was repeated at all wavelengths of interest. More details about the calibration procedure can be found in Experimental section.

We investigated three different lead iodide and bromide perovskites, that will be referred to as MAPB ($CH_3NH_3PbBr_3$), MAPI ($CH_3NH_3PbI_3$) and mixed perovskite ($((CH_3NH_3)_{1-x-y}(CH(NH_2)_2)_xCs_yPbI_{3-z}Br_z$), a mixed-cation, mixed-halide variant that is successfully applied in solar cells.[17] All samples were thin films, spin-coated on glass and covered with a protective poly (methyl methacrylate) (PMMA) layer. The film thickness was around 100 nm, comparable to the penetration

depth of light at the excitation wavelength, resulting in minimal spatial inhomogeneities in the carrier density across the sample depth (see Fig. S1, ESI†). The angular dispersion of the emission is assumed to be Lambertian, namely with intensity proportional to $cos\theta$, where θ is the angle between the normal to the surface and the photon direction, as schematically represented by the green lobe in Fig. 1 (a). Only the light emitted within a small solid angle along the backward direction perpendicular to the film surface is detected, highlighted as the yellow cone in Fig. 1 (a).

A set of absolute TRPL measurements as a function of the injected carrier density n_0 was performed for each sample under study. We then considered $r_{\mathrm{ext},0}$, *i.e.*, the total number of photons emitted per unit time and unit film volume which eventually escape the film from both the front and back film surfaces after multiple emission and absorption processes. We obtain $r_{\mathrm{ext},0} = (2\pi/d)PL_0$, where d is the film thickness and 2π accounts for the effective emission solid angle of the two emitting surfaces under the assumption of a Lambertian angular dispersion. The validity of this latter hypothesis was confirmed by photoluminescence measurements in an integrating sphere, whose results will be discussed in the next paragraph. By exploiting the relation between $r_{\mathrm{ext},0}$ and the injected carrier density n_0,

$$B_{\mathrm{ext}} = r_{\mathrm{ext},0}/n_0^2, \quad (1)$$

we could determine the external radiative bimolecular recombination constant B_{ext}. The results are reported in Fig. 1(b), where the quadratic dependence of $r_{\mathrm{ext},0}$ from n_0 is confirmed by B_{ext} being approximately constant over a wide range of excitation densities, with deviations at higher densities due to saturation effects. The average B_{ext} values are reported on top of the graph. The fact that B_{ext} does not depend on the excitation fluence also demonstrates that the residual background doping is negligeable with respect to the injected carrier concentrations, even at the lowest fluences we have explored.

In Fig. 1(d-e) are shown two PL spectrograms of a MAPB film: spectrogram (d) was recorded in a vacuum chamber filled with air after a prolonged film illumination at atmospheric pressure, while (e) was taken holding the sample at low pressure. Photo-healing increases PL decay times up to more than 100 ns, while lifetime is reverted to less than 10ns when the sample is kept in vacuum. This increased non-radiative lifetime is a well-known phenomenon, resulting in an increase in the time-integrated PL and consequently in the photoluminescence quantum yield (*QY*).[42–46] The radiometric measurements demonstrates that the absolute radiance at $t = 0$ (PL_0), which is proportional to B_{ext}, is actually not affected by photohealing, showing no evident correlation between the radiative recombination rate constant derived from equation (1) and the characteristic time of the PL decay. To exclude possible ultrafast decays of the excited population, also femtosecond differential transmission measurements have been performed on the MAPB film kept in vacuum, as reported in Fig. S2, ESI†.

B_{ext} also depends on film interfaces, which can be suitably designed to enhance the fraction of light emitted externally, as is often done in light emitting devices. The intrinsic recombination constant of the material is $B_{\mathrm{int}} = r_{\mathrm{int},0}/n_0^2$, where $r_{\mathrm{int},0}$ is the spontaneous photon emission rate per unit of volume inside the bulk material. In the limit of isotropic internal light emission, $r_{\mathrm{int},0}$ can be estimated from the knowledge of PL_0 alone, namely the external light radiance emitted perpendicularly to the film surface, whose value would not be affected by the angular dispersion possibly deviating from a Lambertian pattern. In the limit of very thin layers, B_{int} reads:

$$B_{\mathrm{int}} \approx \frac{4\pi\tilde{n}_{\mathrm{film}}^2}{1-R}\frac{PL_0}{d\,n_0^2} \quad (2)$$

where $\tilde{n}_{\mathrm{film}}$ represents the film refractive index, R the sample reflectance at the PL emission wavelength. According to our definition of B_{ext}, it can be shown that $B_{\mathrm{int}} = 2\tilde{n}_{\mathrm{film}}^2/(1-R)\,B_{\mathrm{ext}}$. We refer to section S3 in ESI† for a detailed analysis of the thermodynamic equations connecting B_{int} to PL_0 and B_{ext}. The values of B_{int} and B_{ext} are reported in Table 1 and Table 2.

Radiative and non-radiative bimolecular decays.

To determine the nature of the processes governing the carrier recombination kinetics in our films, we first analysed the temporal PL decays at different excitation fluences. In Fig. 2 (a-c) Markov plots are shown,[13] obtained by shifting each PL transient along the time axis until it overlaps with the decay curve corresponding to the next higher fluence. In each of the investigated films of MAPI, mixed perovskite and MAPB, the resulting PL transients merge with each other, identifying a single decay curve extending over more than six orders of magnitude in the PL instantaneous intensity. The existence of a single decay curve for each sample implies that, at any time after excitation, the PL radiance does not depend on the previous history of the excited state, but only on the instantaneous value of the carrier density n, the key feature defining a Markov process.

The Markovian nature of the decay allows us to neglect contributions of non-Markovian kinetics in the analysis of the PL transients, such as excitation-induced saturation of electronic traps, which would introduce trapped populations as further excited-state parameter, or the kinetics of carrier diffusion,

Table 1: Radiative and non-radiative bimolecular decay rate constants.

	B_{ext} ($\mathrm{cm^{-3}s^{-1}}$)	k_2 ($\mathrm{cm^{-3}s^{-1}}$)
MAPB	$1.1 \cdot 10^{-11}$	$1.1 \cdot 10^{-10}$
MAPI	$4.0 \cdot 10^{-12}$	$2.7 \cdot 10^{-10}$
mixed MAPI	$7.5 \cdot 10^{-12}$	$1.6 \cdot 10^{-10}$

External radiative bimolecular recombination constant B_{ext} is obtained by applying equation (1) to experimental data reported in Fig. 1(b). The second order rate constant k_2 is obtained from the global fit of PL decays, represented with blue squares in Fig. 2 (d-f).

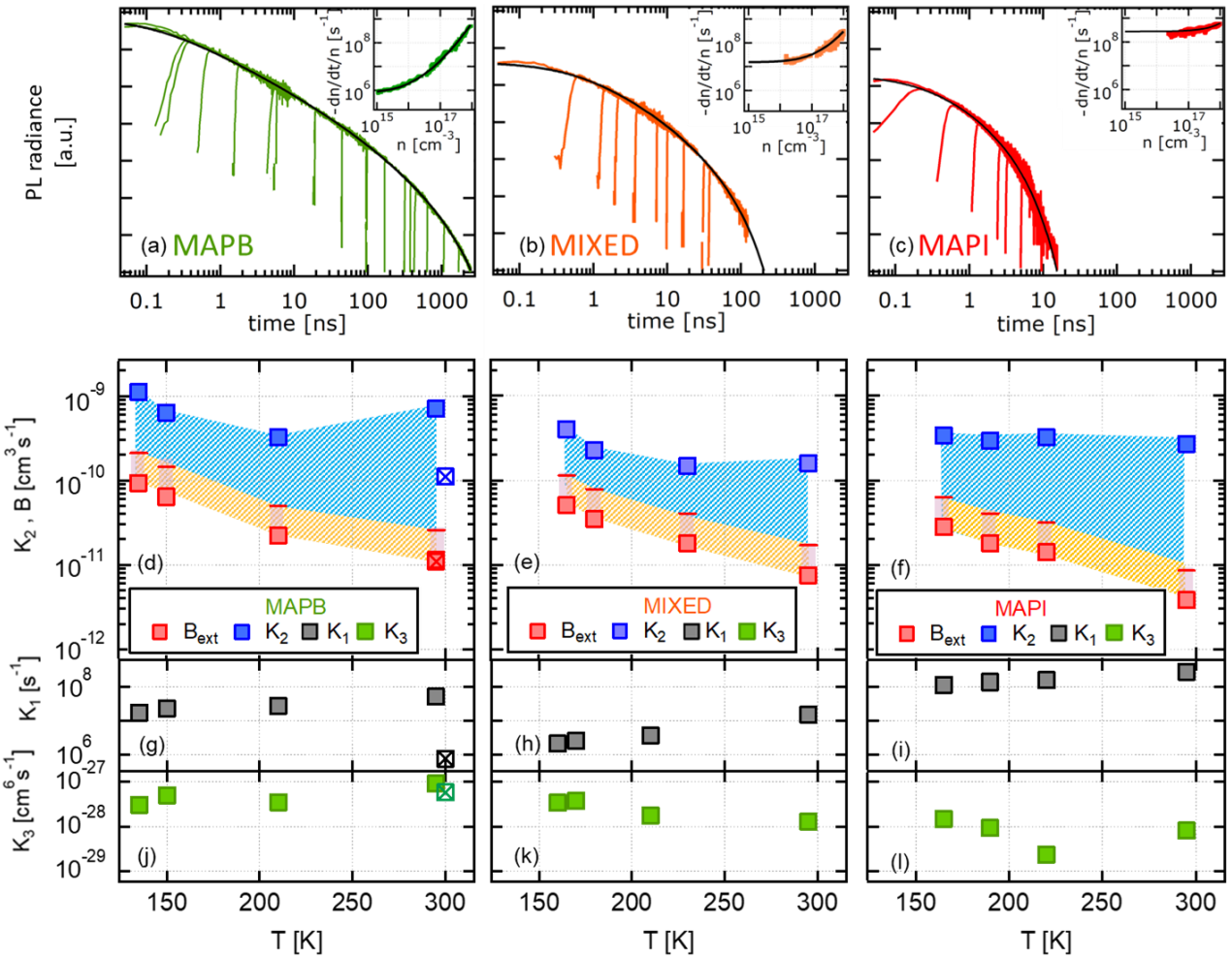

Fig. 2: Upper panel (a-c): Markov plot of the PL time decays in log-log scale, obtained shifting the initial time of each decay to match the PL radiance curves at higher excitations. Black curves represent the result of the global fit with an ordinary differential equation with a common set of k_1, k_2 and k_3 coefficients for all the decay profiles of the same sample. The insets in the upper right corner of each graph show the decay rate (the inverse of the decay time) versus the injected carrier density in log-log scale: experimental data are reported as coloured dots, while the black curve represents the fitted decay equation. Lower panel: Comparison between B_{ext} and k_2 at different temperatures in the range 130K - 300K for MAPB (d), mixed perovskite (e) and MAPI (f). The values of B_{ext}, obtained from absolute PL_0 radiances, are represented with red squares, while horizontal red segments represent the highest achievable B_{ext}, under the assumption that all the light waveguided along the film plane ultimately leaves the sample. The range of B_{ext} values resulting from only a partial extraction of the waveguided light is represented by the yellow areas. The global fit coefficients k_1, k_2 and k_3 are reported in graphs (g-i), (d-f) and (j-l) respectively, with the light-blue region in (d-f) highlighting the difference between maximum B_{ext} and k_2 for the same set of measurements. In (d) we report with crossed squares the results for MAPB after photo-healing treatment, with the values of B_{ext} before and after photo-healing not distinguishable since overlapped.

which would require the introduction of a spatial population profile spreading over time.[12]

The charge carrier concentration n being the only relevant parameter, the transient PL decay could be modelled by solving the standard ABC rate equations, with three elementary processes, related to monomolecular (rate constant k_1), bimolecular (rate constant k_2) and trimolecular Auger recombination (rate constant k_3):

$$\frac{dn}{dt} = -k_1 n - k_2 n^2 - k_3 n^3. \quad (3)$$

A global fit was then performed on all the PL time profiles recorded for each sample. The squares of the solutions for the rate equations $n^2(t) \propto PL(t)$, reported as solid black curves in Fig. 2 (a-c), reproduce the Markov recombination curve with remarkable accuracy in all the three perovskite films, across six orders of magnitude in photoluminescence signal amplitude and five decades in time span (30 ps to 3μs). Such an agreement ensures us that the rate coefficients are not depending on the carrier density, otherwise the ABC model would not be able to provide a global fit.

The three processes contribute differently to the total decay rate, with the third order k_3 term being the dominant one in the first few tens of ps after excitation at the highest fluence, then the bimolecular $k_2 n$ rate taking over for several hundreds of picoseconds, and finally, when the density n is substantially reduced, the monomolecular trapping rate causing the long mono-exponential decay, that may extend for over a microsecond. The one-to-one correspondence between the carrier density n and time t allows to invert the solution of rate equations and plot the decay rate (*i.e.*, the inverse of the decay time), namely $(-dn/dt)/n$, as a function of the density n, as shown in the insets of Fig. 2 (a-c). The slope in log-log scale directly indicates the leading recombination order, 1 at low densities, increasing to 2 and then 3 at higher carrier densities.

The main takeaway from the rate equation analysis, shown in Fig. 2 (d-f), is that the value of the bimolecular k_2 constant extracted from the PL dynamics is much higher than the value of the radiative constant B_{ext}. In other words, we find a dominant contribution to k_2 that comes from non-radiative bimolecular annihilation processes, which is not affecting B_{ext}. Our conclusion is strengthened by comparing the results obtained before and after photo-healing of the MAPB film (crossed squares in Fig. 2(d)): we found a reduction by a factor ~7 of k_2 with respect to the value before treatment, without any concomitant change in the radiative decay constant B_{ext}, whose value is indistinguishable before and after photo-healing. A non-radiative contribution to k_2 requires going beyond a conventional annihilation process of the electron-hole pair, in which the energy of the couple is transferred to the photon, according to the scheme $e + h \longrightarrow \hbar\omega$. One possibility is non-radiative recombination of free carriers through shallow traps, i.e. traps with energy depth smaller than the energy difference between the band edge and the quasi-Fermi level. In such a case, the trap-assisted recombination would still be bimolecular, because the trapped carrier population is in equilibrium with the free carrier population. Another mechanism could be trap-mediated Auger recombination, which involves two free charges and one trapped.[47] An alternative explanation has been recently proposed, which is peculiar of metal halide perovskites and naturally results from considering that the excited state contains both charged carriers and neutral bright excitons, the former constituting the majority population and the latter the minority one.[13]

Since all decay rate constants are known to depend on temperature, our analysis was extended from 300K down to 130K (see Fig. S4 and S5, ESI†). Fig. 2 (d-l) show the best values of k_1, k_2 and k_3 coefficients resulting from the global fits. The values of k_2 (blue squares) are to be compared with the values of B_{ext} (red squares) extracted from absolute PL radiances coming from the same sets of measurements, whose room-temperature values are reported in Table 1.

At all temperatures and for all the samples under analysis the second order recombination constant k_2 is much higher than B_{ext}. The horizontal segments above the red squares represent the maximum values of B_{ext} that can be achieved depending on the extraction efficiency of photons generated inside the film, that can be up to $\tilde{n}_{\text{cap}}^2$ times higher, with $\tilde{n}_{\text{cap}}$ the refractive index of the capping layer on top of the surface (see Fig. 3(b) and Fig. S6 ESI† for more details). The possible range of values that can be taken by B_{ext} is represented by the vertical pink bars in Fig. 2 (d-f), with interpolated regions depicted as yellow shaded areas. It is evident that, even accounting for different photon extraction efficiencies, the discrepancy between B_{ext} and the corresponding k_2 can exceed one order of magnitude even at low temperatures, as highlighted also by the blue-shaded regions in Fig. 2 (d-f).

Fig. 3 (a) reports the *QY* measured under pulsed excitation, where *QY* data (empty squares) are obtained by integrating over time the transient PL radiance, divided by the injected carrier density n_0 and multiplied by 2π to account for the overall emission form the front and back film surfaces. As an independent validation, we measured the *QY* of the MAPB sample with an integrating-sphere PL set-up (Fig. 3 (b)), under the same pulsed excitation as in the absolute radiance measurements. The results, represented by black squares in Fig. 3 (a), are consistent with those obtained in the radiometric time-resolved PL setup assuming a Lambertian angular dispersion of light emission (see S6 ESI† for integrating sphere measurements and the contribution to the external PLQY by light propagating along the film plane).

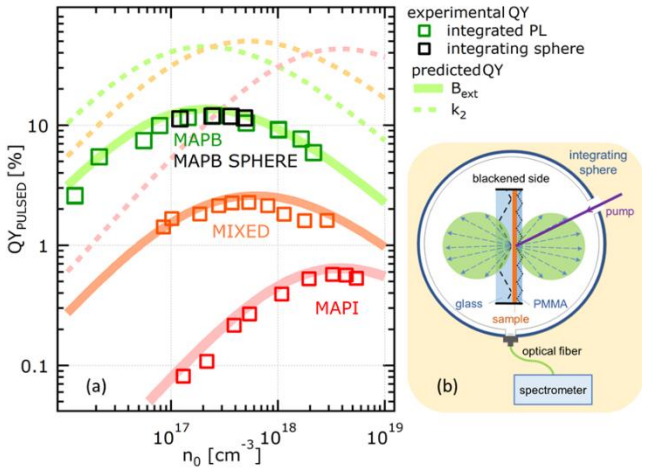

Fig. 3: (a) *QY* measured under pulsed excitation as a function of injected carrier density n_0 at room temperature. Green, orange, and red squares are estimated from the time-integral of calibrated radiance measurements of MAPB, mixed perovskite and MAPI, respectively. Black squares show the results of measurements on MAPB using the setup sketched in inset (b), keeping the sample under the same pulsed excitation inside an integrating sphere to collect emission (sizes are not to scale for sake of clarity). The edges of the glass were blackened to block the light propagating in the plane of the glass or PMMA. Emission from MAPI and mixed perovskite samples was so feeble that could not be measured with the integrating sphere, due to a limitation in the maximum exposure time. In (a) solid lines are representing the *QY* versus n_0 computed as explained in the main text, considering B_{ext} as the radiative decay rate, while dashed lines represent the values of *QY* if considering k_2 in place of Bext.

The solid curves in Fig.3(a) represent the *QY* estimated as $QY = (1/n_0)\int_0^\infty B_{\text{ext}}\, n^2(t)\, dt$. The instantaneous carrier density $n(t)$ was calculated from the rate equation (3) with the initial condition $n(0) = n_0$, using the decay rate constants k_i from the global fit analysis. Looking at the *QY* trend versus n_0 in Fig. 3(a), a bell-shape can be recognised, with the *QY* being limited by the monomolecular trapping process at lower excitation fluences, and by Auger recombination at higher fluences. In Fig. 3 (a), we also show the *QY* (dashed lines) calculated as $(1/n_0)\int_0^\infty k_2 n^2(t)\, dt$, i.e., assuming that all bimolecular decays are radiative. The resulting *QY* largely exceed the experimental one, confirming that $k_2 \gg B_{ext}$.

Reciprocity law between light emission and absorption

The analysis performed so far on different perovskite films does not require any assumption on the nature of the light-emitting species. In this section, the absorptance and photoluminescence spectra of perovskite films are analysed to identify which are the excitations responsible of photon emission and their contributions. The starting point of our analysis, based on the reciprocity between photon absorption and emission (in the non-quantum-degenerate Boltzmann

limit), is the Planck law for a black body, generalized by Würfel to extend its validity to semiconductors:[48]

$$r_{\hbar\omega,\mathrm{ext}} = \frac{2\pi\, e^{\frac{\mu}{kT}}}{4\pi^3\hbar^3c_0^2 d}a(\hbar\omega)[\hbar\omega]^2 e^{-\frac{\hbar\omega}{kT}} \quad (4)$$

$$r_{\hbar\omega,\mathrm{int}} = \frac{4\pi\, e^{\frac{\mu}{kT}}}{4\pi^3\hbar^3c_0^2} n_r^2(\hbar\omega)\alpha(\hbar\omega)[\hbar\omega]^2 e^{-\frac{\hbar\omega}{kT}}. \quad (5)$$

Here $r_{\hbar\omega,\mathrm{ext}}$ and $r_{\hbar\omega,\mathrm{int}}$ are the external and internal spontaneous photon emission rate per unit of photon energy $\hbar\omega$ and of film volume. In the above relations $a(\hbar\omega)$ is the film absorptance, $\alpha(\hbar\omega)$ the absorption coefficient, $\tilde{n}_r(\hbar\omega)$ the real index of refraction and μ the chemical potential of the electron and hole pairs, namely the split of the quasi Fermi level. If electronic excitations are only created by thermal energy, $\mu = 0$ holds and eq. (5) recovers the Van Roosbroeck–Shockley relation, which simply states that, according to the principle of detailed balance, the spontaneous photon emission rate equates the absorption rate of thermal radiation at any given photon energy.[49] This reciprocity law is widely used to estimate the radiative limit of the open circuit voltage of a solar cell,[50,51] and specifically of perovskite-based photovoltaic devices.[52] Since $a(\hbar\omega)$ and $\alpha(\hbar\omega)$ were measured in a spectrophotometer, as described in Experimental section, the integration of equations (4) and (5) allows us to determine the overall external and internal thermal emissions, respectively. The factor 2 in the numerator of (4) is due to the contributions coming both from back and front surface (more details on the derivation can be found in S3, ESI†). We used these equations to infer the internal radiative bimolecular recombination constant B_{int}, and to distinguish the contributions resulting from the decay of excitons and of free electron-hole pairs.

We first checked whether the generalized Planck law (4) reproduced the spectrum of spontaneous emission in our films, focusing on the experimental data of MAPB, whose absorption spectrum features a pronounced contribution from excitonic transitions as can be seen in Fig. 4 (the same analysis for MAPI is reported in S7, ESI†). The central graph in Fig. 4 shows a good agreement between the measured PL spectrum PL_{exp} (green) and the spectrum obtained by applying equation (4), r_{ex} (yellow). The low-energy shoulder in the experimental PL spectrum is also reproduced, indicating that it may be arising from ground-state defects. This positive check ensures us that the same states and transitions are involved in photon absorption and emission.

As a second step, the absorption coefficient was fitted with Elliott's law for excitonic band-edge absorption to disentangle excitonic transitions from band-to-band ones (see discussion in S8, ESI†). Once the two absorption contributions were fixed, we calculated the overall internal emission $r_{\hbar\omega,\mathrm{int}}$ and the contributions resulting from exciton and unbound electron-hole pair recombination. As shown in Fig. 4, most photons are emitted following exciton annihilation.

We may now estimate the predicted recombination rate as:

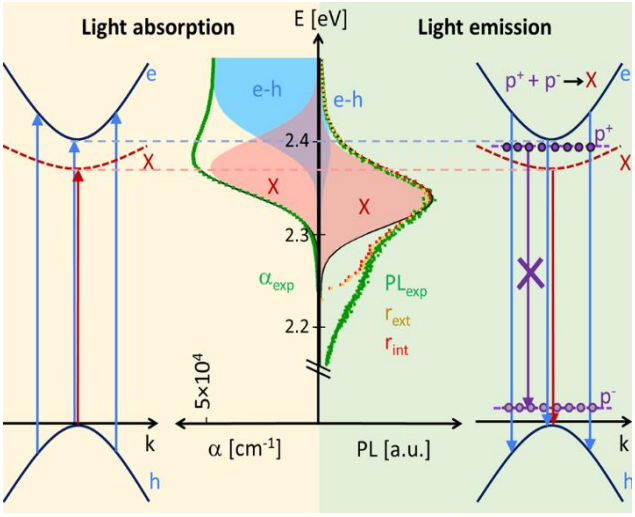

Fig. 4: Sketches of light absorption (left) and emission (right) processes, with black and dashed red curves representing electron-hole and exciton bands, respectively; purple circles on the right represent polaronic states. Graphs in the centre compare experimental and theoretical absorption coefficient α and PL spectra for MAPB film. Left graph: theoretical absorption coefficient (black) resulting from the contributions of exciton (pink filling) and valence-to conduction band transitions (light blue filling), in good agreement with experimental absorption coefficient spectrum (green trace). Right graph: experimental PL spectrum (PL_{exp}, green) compared with the external r_{ext} (yellow) and internal r_{int} (red) luminescence estimated, respectively, from absorptance and absorption spectra through the generalized Planck laws. As the investigated film was very thin, the spectral shapes of r_{ext} and r_{int} are indistinguishable. The close correspondence between PL_{exp} and r_{ext} confirms that the same states are involved in absorption and emission processes. PL spectrum estimated from theoretical absorption coefficient through the same generalized Planck law is represented in black, with exciton and band-to-band contributions also shown as pink and light blue filled areas, respectively.

$$B_{\mathrm{int}} = \frac{\int_0^\infty r_{\mathrm{sp,int}} d(\hbar\omega)}{n_{\mathrm{th}}^2}, \quad (6)$$

i.e., by integrating equation (5) and dividing it by the square of the thermal population:

$$n_{\mathrm{th}} \sim 2(2\pi mkT/h^2)^{3/2} e^{-E_g/2kT}, \quad (7)$$

where m is the effective mass of photoexcitations and E_g the energy gap (see discussion S9, ESI† for more details on the calculation of B_{int} and n_{th}). The resulting values are reported in Table 2: the value predicted from absorption with the described calculation turned out to be 80 times larger than the experimental value of B_{int}, directly measured from PL without any assumption on the nature of the excited state population. Similar results were also found for MAPI (Table 2). Our result considering the free-carrier contribution only to B_{int}, as assessed from the Van Roosbroeck–Shockley relation, is in good agreement with values reported in literature.[21,27] Yet, the approximation of neglecting the radiative recombination of excitons is not justified in the light of the previous discussion (see Fig. 4).

Discussion

Rigid-lattice assumption versus polaron formation

The excited-state picture emerging from our set of optical measurements in MAPI and MAPB is characterized by: *i)* a sharp absorption edge and an excitonic spectral feature with absorption coefficient in excess of 10^4 cm^{-1}; *ii)* spontaneous light emission resulting from the same optical transitions involved in the absorption spectrum; *iii)* a quadratic dependence of the PL intensity on the density of photoexcitations, and most important *iv)* a bimolecular recombination of carriers mostly nonradiative in nature, with a radiative rate ~ 80 (in MAPB) and ~ 40 (in MAPI) times smaller than those expected for a population of excitons and free carriers.

At first sight, point *ii)* and *iii)* could appear in contrast with the monomolecular radiative decay of excitons.[21] Yet, as discussed in reference [13], the quadratic dependence of the PL intensity can be naturally explained by assuming that charged carriers represent the majority population, while excitons are minority bright species, formed following bimolecular pairing of charges with opposite sign (see Fig. 4a in reference [13] for a scheme of decay processes). On one side the generalized Planck law in hybrid perovskites accurately reproduces the emission spectrum, on the other hand the measured B_{int} is much lower than the value expected from the optical emission of excitons and free electron-hole pairs, the excited species created upon absorption. A re-examination of the evaluation of B_{int} is therefore warranted, particularly of the charged carrier effective masses and bandgap energies employed to calculate the value of the thermal population n_{th}. There exists a growing body of experimental evidence in literature indicating that the perovskite lattice relaxes around electrons and holes to form large charged polarons.[53–55] Lattice reorganization in the excited state to form charged polarons shifts the chemical equilibrium between excitons and charged carriers towards these latter. In other words, the presence of polarons reduces the concentration of light-emitting excitons, being polarons heavier and closer in energy to excitons with respect to lattice-unrelaxed charges. As a result, a thermal population constituted by polarons is considerably larger than what obtained under rigid lattice assumption.

Table 2: Internal radiative decay rates from PL and from absorption

	B_{int} $(\mathrm{cm}^{-3}\mathrm{s}^{-1})$	
	measured from PL	**Calculated from abs**
MAPB	1.8 10^{-10}	1.5 10^{-8}
MAPI	6.3 10^{-11}	2.2 10^{-9}

Values for the internal bimolecular radiative recombination rate coefficient B_{int} derived from the calibrated measurement of the PL radiance through equation (2), or estimated from the absorption coefficient through the generalized Planck law, using equations (6) and (7), with effective masses $m_e = 0.22\ m_0$, $m_h = 0.23\ m_0$ for electron and hole respectively in MAPI[27] and $m_e = 0.277\ m_0$, $m_h = 0.245\ m_0$ in MAPB[56] (see S9, ESI†). The bandgaps extracted from absorption through Elliott formula are $E_g = 1.648\ eV$ for MAPI and $E_g = 2.40\ eV$ for MAPB.

A simple estimate based on the Feynman polaron model gives a thermal population enhancement factor of 58.5 for MAPI (details of the calculation are in S10, ESI†), not far from the factor 40 suppression in the radiative coefficient reported in Table 2.

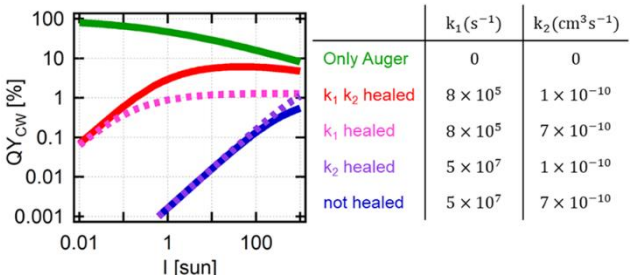

Fig. 5 Expected quantum yield under continuous wave excitation (QY_{CW}) versus the intensity of the applied sunlight, distinguishing different scenarios where $k_1$and k_2 are affected or not by photohealing. The corresponding values of $k_1$and k_2 are reported in the table on the right, for each QY_{CW} curve. The blue solid curve (not healed) represents the QY_{CW} obtained with values of k_1 and k_2 from the fit of MAPB PL decay without photo-healing. The red curve is obtained considering the values of k_1 and k_2 after photo-healing. Pink and purple dashed curves are hypothetical results that would be obtained if photo-healing was affecting only k_1 or k_2, respectively. Green solid line finally represents the ideal case in which both k_1 and k_2 are negligible, and Auger recombination is considered as the only intrinsic effect.

The physics of electron and hole polarons in hybrid perovskites was recently simulated through advanced ab initio molecular dynamics,[40] where it was found that the spatial overlapping between electrons and holes in MAPI is reduced by about two-orders of magnitude following lattice relaxation. The degree of overlap determines the rate at which polarons of opposite sign pair to form bright excitons.

The results of these simulations appear therefore consistent with our experimental results, the bimolecular radiative decay constant B_{int} being in MAPI (MAPB) 40 (80) times smaller than estimates under the assumption of no lattice deformation in the excited state.

Effects on the prediction of solar cell performances

The competition between radiative and nonradiative bimolecular recombination plays a key role in determining the photoconversion efficiency of perovskite solar cells and is central for approaching the Shockley-Quessier limit. The maximum open circuit voltage can be achieved in the pure radiative limit, and depends on the ratio between the injection rate of electron-hole pairs due to absorption of solar and thermal radiation.[52] As such, the radiative limit efficiency is independent of the actual radiative decay rate. Conversely, every drop of a factor 10 in the *QY* leads to an additional 60 meV voltage loss. For this reason, the very low radiative recombination rate of hybrid perovskites necessarily requires an even slower nonradiative decay to maximize the *QY*.

Fig.5 illustrates the expected quantitative effects of photohealing of the the MAPB film on the CW emission quantum yield (QY_{cw}) under steady-state excitation with sunlight, i.e., how close a solar cell based on such materials may operate to the radiative limit. The rate equation is solved by equating the total decay rate $k_1 n + k_2 n^2 + k_3 n^3$ to the carrier generation rate $G = \int_0^\infty I \frac{\mathrm{S}(\hbar\omega)}{\hbar\omega} \alpha(\hbar\omega) d(\hbar\omega)$ due to the absorption of sunlight ($\mathrm{S}(\hbar\omega)$ is the AM 1.5G spectrum, 100mW/cm^2, and I is the applied sunlight intensity measured in

suns) by the MAPB film with absorption coefficient $\alpha(\hbar\omega)$. Once the carrier density $n(I)$ is obtained as a function of the applied light intensity, $QY_{\mathrm{cw}} = B_{\mathrm{ext}}n^2/(k_1 n + k_2 n^2 + k_3 n^3)$ is obtained as the ratio between radiative and total decay rates. In the MAPB films we studied, light irradiation under atmospheric pressure reduced the monomolecular decay constant k_1 by a factor $\sim$70, and the second order one, k_2, by a factor $\sim$ 7, as reported in the table on the right side of Fig. 5. The solid blue curve is calculated with the values of k_1 and k_2 of MAPB film before photo-healing, while the red one is obtained from the values of k_1 and k_2 reduced due to photo-healing. The dashed pink and purple curves are calculated considering the effect of photo-healing on k_1 or k_2 only, respectively. From this projection, it is evident that the increase in QY_{cw} following photo-healing is resulting from the synergy between both contributions of k_1 and k_2, the decrease of the monomolecular decay rate being not sufficient to explain the total improvement in QY_{cw}. The green line in Fig. 5 also shows the highest QY_{cw} that could be obtained if Auger recombination, assumed as intrinsic, would be the only nonradiative decay channel. This analysis points to the fact that small k_1 values in high quality samples allow the build-up of a large carrier density, which however in turn enhances the contribution of the bimolecular nonradiative decays. The contribution of k_2 to the overall non-radiative decay rate under 1 sun illumination may therefore become important, even the dominant one, and needs to be dealt with to approach the radiative Shockley-Quessier limit. To create the range of injected carrier densities considered in this work under cw illumination, intensities significantly greater than 1 sun are needed, causing significant temperature variations in perovskite films and sample instabilities; for such reasons calculations in Fig. 5 could not be supported with experimental data.

Conclusions

In this work we determined the radiative recombination rates in 3D hybrid perovskite thin films by setting up a radiometric time-resolved PL measurement. The measured radiative recombination constants are much lower than the ones estimated from the absorption spectrum through the Van Roosbroeck–Shockley relation under the assumption that only excitons and free carriers are present, pointing to the existence of a majority population of dark excitations, possibly large polarons. The bimolecular radiative decay constant B_{ext} is also substantially smaller than the second order constant k_2 obtained from the PL decay dynamics, demonstrating that bimolecular decay in hybrid perovskites is mostly non-radiative and extrinsic in nature. Photo-healing is found to reduce the second order nonradiative decay channel (k_2) in addition to the first order one (k_1). The findings reported here impose stringent limits on improving the open circuit voltage and efficiency of solar cells, since unwanted, non-radiative decay rates need to be suppressed much further than previously thought.

Experimental

Samples preparation

All the film depositions were performed inside a nitrogen-filled glove box. Bromide, Iodide and mixed I-Br perovskite thin films were fabricated by one-pot, two-steps and antisolvent spin coating deposition, respectively.

The $CH_3NH_3PbBr_3$ (MAPB) solution was prepared by dissolving MABr+$PbAc_2$*$3H_2O$ with a molar ratio 3:1 in dimethylformamide (DMF) and a final concentration of 0.5 M. The films were deposited on a glass slide at 6000 rpm for 60 s and annealed at 100°C for 5 minutes.

The $CH_3NH_3PbI_3$ (MAPI) film was prepared by spinning a 0.5 M PbI_2 solution in DMF on a glass slide at 6000 rpm for 30 s followed by annealing at 80°C for 10 min. Then some drops of MAI dissolved in isopropanol (10 mg/ml) were cast on the film and left it react for 2 minutes before the spinning. The MAPI film was annealed at 100°C for 30 min and then washed with isopropanol with a subsequent annealing at 100°C for 1 h.

The $MA_{1-x-y}FA_xCs_yPbI_{3-z}Br_z$ perovskite film was prepared with a 0.3 M precursor solution of FAI, MABr, CsI, PbI_2 and $PbBr_2$ with final stoichiometry $Cs_{0.05}FA_{0.81}MA_{0.14}PbI_{2.55}Br_{0.45}$ in a mixed solvent of DMF and dimethyl sulfoxide (DMSO) with a volume ratio of 4:1. The spin coating procedure in this case is assisted by an antisolvent: first, two drops of solution were spun at 2000 rpm for 10 s with an acceleration of 200 rpm/s, then at 4000 rpm for 20 s with an acceleration of 1000 rpm/s. Ten seconds before the end of the whole spinning cycle, 100 µL of chlorobenzene were dropped on the substrate. The substrate was then thermally treated at 100 °C on a hotplate for 10 min. After the annealing, all the films were coated with a layer of PMMA dissolved in chlorobenzene.

Calibrated time-resolved PL measurements

Our ultrafast pulsed laser source was a Ti:sapphire regenerative amplifier (Coherent Libra) delivering 100-fs long pulses at 794 nm, with energy up to 4mJ and 1KHz repetition rate. The frequency conversion of the pulses was obtained with an optical parametric amplifier (TOPAS 800 from Light Conversion) equipped with nonlinear crystals, providing the excitation wavelength of 430nm for MAPB and 630nm for MAPI and mixed MAPI. Time-resolved detection system was constituted of a grating spectrometer (Acton 2300i) coupled to a streak camera (Hamamatsu C10910). In the low-temperature measurements the sample was kept inside a cryostat (Janis ST-500). Images of the laser spot in the plane of the sample were detected with a visible camera (Thorlabs DCC1545M).

The calibration procedure to obtain the absolute intensity of the PL signal was based on the determination of quantum efficiency of the spectrometer and streak camera detection system, i.e., by measuring the signal generated by laser pulses of known intensity under the very same operating conditions and streak camera settings used for the PL. The ultrafast pulsed laser source (Coherent Libra + TOPAS) was set at the wavelength range of the PL emission (530 nm for MAPB, 760 nm for MAPI and mixed perovskite) and was first measured with a power meter - photodiode system (PD300R-UV by Ophir Photonics).

The laser pulses were then attenuated with calibrated neutral optical densities filters (the actual OD value for each filter when illuminated by femtosecond laser pulses was measured) and sent into to the streak camera, keeping both horizontal and vertical slits wide open, so that all the incoming power was collected. Comparing the spectrally and time integrated counts per frame with the injected number of photons per pulse we could determine the quantum efficiency in the spectral region of the PL emission, i.e., $QE = 2.8 \cdot 10^{-3}\ counts\ /photon$ at 530nm and $QE = 3.3 \cdot 10^{-4}\ counts\ /photon$ at 760nm. To independently check the wavelength dependence of the calibration, the relative response was tested in the spectral region of interest using a radiometric calibrated lamp (Ocean Optics HL-3P-Cal) as source.

To evaluate the fraction of collected emission with respect to the Lambertian PL emitted from the surface, we fixed the solid angle of collection of the PL by placing an iris after the PL collection lens. By varying the iris aperture radius, the detected signal was verified to scale linearly with the collection solid angle.

Absorptance measurements

Optical absorption spectra of thin films in the UV-vis range was measured with a dual-beam spectrophotometer equipped with an integrating sphere accessory (Agilent Technologies Cary 5000 UV–vis–NIR) in order to avoid losses due to diffused transmission and reflection, collected with an hemispherical configuration.[57]

Integrating sphere measurements

Reflection/Transmission integrating sphere (LabSphere) with 6-inches diameter connected via an optical fiber to high resolution spectrometer (Photon Control SPM-002-ET64).

Author Contributions

Samples were prepared by R.P., F.L., L.W. and D.M. Film characterization was performed by F.L., L.W., A.G-L. and D.M. A.S., R.P., M.S. and A.M. set up the calibrated PL radiance apparatus and performed the corresponding measurements. D.M., S.L. and F.Q. performed absorptance measurements. A.S. performed the measurements with integrating sphere. G.B. proposed the original idea of the PL calibrated radiometric measurements. A.F. did the calculations for the polaron model. M.A.L. Critically discussed the interpretation of measurements. A.S., F.Q., M.S. and G.B. analysed the data and wrote the manuscript, finalized with contributions from all the authors. This work was coordinated by M.S. and G.B. All the authors approved the final version of the paper.

Conflicts of interest

There are no conflicts to declare.

Acknowledgements

The authors acknowledge access to research infrastructure in CeSAR—Centro Servizi di Ateneo per la Ricerca—at Università degli Studi di Cagliari and thank Dr. M. Marceddu for technical assistance. A.S. was supported by PON "Ricerca e Innovazione" 2014–2020 - Fondo Sociale Europeo, Attraction and International Mobility - AIM1809115-2, Linea 2.1. This work was funded by Regione Autonoma della Sardegna through PO-FSE Sardegna 2007–2013, L.R. 7/2007, "Progetti di ricerca di base e orientata," Projects Nos. CRP3-114, CRP-17571, CRP-18353, CRP-18013, and CRP-24978, and through Delibera CIPE n. 31 del 20.02.2015 e deliberazione n. 52/36 del 28.10.2015 "Piano Strategico Sulcis," through Project Nos. SULCIS-820889 and SULCIS-820947, as well as by MUR (Italian Ministry of University and Research) through PRIN PERovskite-based solar cells: toward high efficiency and long-term stability (PERSEO), project id 20155LECAJ. The work was also supported by Fondazione di Sardegna through project 2F20000210007 "Perovskite materials for photovoltaics." A.F. thanks Project PRIN 2017 "TOPSPIN", funded by Italian Ministry of University and Research (MUR).

References

1 J.-P. Correa-Baena, M. Saliba, T. Buonassisi, M. Grätzel, A. Abate, W. Tress and A. Hagfeldt, *Science*, 2017, **358**, 739–744.

2 J. Chen and N. G. Park, *Adv. Mater.*, 2019, **31**, 1–56.

3 N. G. Park and H. Segawa, *ACS Photonics*, 2018, **5**, 2970–2977.

4 D. Luo, R. Su, W. Zhang, Q. Gong and R. Zhu, *Nat. Rev. Mater.*, 2020, **5**, 44–60.

5 M. Green, E. Dunlop, J. Hohl-Ebinger, M. Yoshita, N. Kopidakis and X. Hao, *Prog. Photovoltaics Res. Appl.*, 2021, **29**, 3–15.

6 K. A. Bush, A. F. Palmstrom, Z. J. Yu, M. Boccard, R. Cheacharoen, J. P. Mailoa, D. P. McMeekin, R. L. Z. Hoye, C. D. Bailie, T. Leijtens, I. M. Peters, M. C. Minichetti, N. Rolston, R. Prasanna, S. Sofia, D. Harwood, W. Ma, F. Moghadam, H. J. Snaith, T. Buonassisi, Z. C. Holman, S. F. Bent and M. D. McGehee, *Nat. Energy*, 2017, **2**, 1–7.

7 J. Peng, D. Walter, Y. Ren, M. Tebyetekerwa, Y. Wu, T. Duong, Q. Lin, J. Li, T. Lu, M. A. Mahmud, O. L. C. Lem, S. Zhao, W. Liu, Y. Liu, H. Shen, L. Li, F. Kremer, H. T. Nguyen, D. Y. Choi, K. J. Weber, K. R. Catchpole and T. P. White, *Science*, 2021, **371**, 390–395.

8 Y. C. Shen, G. O. Mueller, S. Watanabe, N. F. Gardner, A. Munkholm and M. R. Krames, *Appl. Phys. Lett.*, 2007, **91**, 144101.

9 J. Cho, J. T. DuBose and P. V. Kamat, *J. Phys. Chem. Lett.*, 2020, **11**, 2570–2576.

10 M. B. Johnston and L. M. Herz, *Acc. Chem. Res.*, 2016, **49**, 146–154.

11 E. V. Peán, S. Dimitrov, C. S. De Castro and M. L. Davies, *Phys. Chem. Chem. Phys.*, 2020, **22**, 28345–28358.

12 J. M. Richter, M. Abdi-Jalebi, A. Sadhanala, M. Tabachnyk, J. P. H. Rivett, L. M. Pazos-Outón, K. C. Gödel, M. Price, F. Deschler and R. H. Friend, *Nat. Commun.*, 2016, **7**, 13941.

13 A. Simbula, R. Pau, Q. Wang, F. Liu, V. Sarritzu, S. Lai, M. Lodde, F. Mattana, G. Mula, A. Geddo Lehmann, I. D.

Spanopoulos, M. G. Kanatzidis, D. Marongiu, F. Quochi, M. Saba, A. Mura and G. Bongiovanni, *Adv. Opt. Mater.*, 2021, **9**, 2100295.

14 A. Kiligaridis, P. A. Frantsuzov, A. Yangui, S. Seth, J. Li, Q. An, Y. Vaynzof and I. G. Scheblykin, *Nat. Commun.*, 2021, **12**, 3329.

15 R. Brenes, D. Guo, A. Osherov, N. K. Noel, C. Eames, E. M. Hutter, S. K. Pathak, F. Niroui, R. H. Friend, M. S. Islam, H. J. Snaith, V. Bulovi, T. J. Savenije, S. D. Stranks, V. Bulović, T. J. Savenije and S. D. Stranks, *Joule*, 2017, **1**, 155–167.

16 F. Staub, T. Kirchartz, K. Bittkau and U. Rau, *J. Phys. Chem. Lett.*, 2017, **8**, 5084–5090.

17 D. Bi, W. Tress, M. I. Dar, P. Gao, J. Luo, C. Renevier, K. Schenk, A. Abate, F. Giordano, J. P. Correa Baena, J. D. Decoppet, S. M. Zakeeruddin, M. K. Nazeeruddin, M. Grätzel and A. Hagfeldt, *Sci. Adv.*, , DOI:10.1126/sciadv.1501170.

18 Y. Yamada, T. Nakamura, M. Endo, A. Wakamiya and Y. Kanemitsu, *J. Am. Chem. Soc.*, 2014, **136**, 11610–11613.

19 R. L. Milot, G. E. Eperon, H. J. Snaith, M. B. Johnston and L. M. Herz, *Adv. Funct. Mater.*, 2015, **25**, 6218–6227.

20 A. R. Srimath Kandada, S. Neutzner, V. D'Innocenzo, F. Tassone, M. Gandini, Q. A. Akkerman, M. Prato, L. Manna, A. Petrozza and G. Lanzani, *J. Am. Chem. Soc.*, 2016, **138**, 13604–13611.

21 M. Saba, M. Cadelano, D. Marongiu, F. Chen, V. Sarritzu, N. Sestu, C. Figus, M. Aresti, R. Piras, A. Geddo Lehmann, C. Cannas, A. Musinu, F. Quochi, A. Mura and G. Bongiovanni, *Nat. Commun.*, 2014, **5**, 5049.

22 W. Rehman, R. L. Milot, G. E. Eperon, C. Wehrenfennig, J. L. Boland, H. J. Snaith, M. B. Johnston and L. M. Herz, *Adv. Mater.*, 2015, **27**, 7938–7944.

23 C. Wehrenfennig, G. E. Eperon, M. B. Johnston, H. J. Snaith and L. M. Herz, *Adv. Mater.*, 2014, **26**, 1584–1589.

24 V. D. Innocenzo, A. Ram, S. Kandada, M. De Bastiani, M. Gandini and A. Petrozza, *J. Am. Chem. Soc.*, 2014, **136**, 17730–17733.

25 C. La-o-vorakiat, T. Salim, J. Kadro, M.-T. Khuc, R. Haselsberger, L. Cheng, H. Xia, G. G. Gurzadyan, H. Su, Y. M. Lam, R. A. Marcus, M.-E. Michel-Beyerle and E. E. M. Chia, *Nat. Commun.*, 2015, **6**, 7903.

26 N. Sestu, M. Cadelano, V. Sarritzu, F. Chen, D. Marongiu, R. Piras, M. Mainas, F. Quochi, M. Saba, A. Mura and G. Bongiovanni, *J. Phys. Chem. Lett.*, 2015, **6**, 4566–4572.

27 C. L. Davies, M. R. Filip, J. B. Patel, T. W. Crothers, C. Verdi, A. D. Wright, R. L. Milot, F. Giustino, M. B. Johnston and L. M. Herz, *Nat. Commun.*, 2018, **9**, 293.

28 V. D'Innocenzo, G. Grancini, M. J. P. Alcocer, A. R. S. Kandada, S. D. Stranks, M. M. Lee, G. Lanzani, H. J. Snaith and A. Petrozza, *Nat. Commun.*, 2014, **5**, 3586.

29 S. Sun, T. Salim, N. Mathews, M. Duchamp, C. Boothroyd, G. Xing, T. C. Sum and Y. M. Lam, *Energy Environ. Sci.*, 2014, **7**, 399–407.

30 M. Habibi, F. Zabihi, M. R. Ahmadian-Yazdi and M. Eslamian, *Renew. Sustain. Energy Rev.*, 2016, **62**, 1012–1031.

31 C. Tablero Crespo, *Sol. Energy Mater. Sol. Cells*, 2019, **195**, 269–273.

32 G. Xing, N. Mathews, S. S. Lim, Y. M. Lam, S. Mhaisalkar and T. C. Sum, *Science*, 2013, **342**, 344–347.

33 L. M. Herz, *ACS Energy Lett.*, 2017, **2**, 1539–1548.

34 T. W. Crothers, R. L. Milot, J. B. Patel, E. S. Parrott, J. Schlipf, P. Müller-Buschbaum, M. B. Johnston and L. M. Herz, *Nano Lett.*, 2017, **17**, 5782–5789.

35 D. Meggiolaro, F. Ambrosio, E. Mosconi, A. Mahata and F. De Angelis, *Adv. Energy Mater.*, 2019, **10**, 1902748.

36 M. J. Schilcher, P. J. Robinson, D. J. Abramovitch, L. Z. Tan, A. M. Rappe, D. R. Reichman and D. A. Egger, *ACS Energy Lett.*, 2021, **6**, 2162–2173.

37 D. Ghosh, E. Welch, A. J. Neukirch, A. Zakhidov and S. Tretiak, *J. Phys. Chem. Lett.*, 2020, **11**, 3271–3286.

38 M. Puppin, S. Polishchuk, N. Colonna, A. Crepaldi, D. N. Dirin, O. Nazarenko, R. De Gennaro, G. Gatti, S. Roth, T. Barillot, L. Poletto, R. P. Xian, L. Rettig, M. Wolf, R. Ernstorfer, M. V. Kovalenko, N. Marzari, M. Grioni and M. Chergui, *Phys. Rev. Lett.*, 2020, **124**, 206402.

39 X. Y. Zhu and V. Podzorov, *J. Phys. Chem. Lett.*, 2015, **6**, 4758–4761.

40 F. Ambrosio, J. Wiktor, F. De Angelis and A. Pasquarello, *Energy Environ. Sci.*, 2018, **11**, 101–105.

41 A. Filippetti, C. Caddeo, P. Delugas and A. Mattoni, *J. Phys. Chem. C*, 2016, **120**, 28472–28479.

42 S. G. Motti, M. Gandini, A. J. Barker, J. M. Ball, A. R. Srimath Kandada and A. Petrozza, *ACS Energy Lett.*, 2016, **1**, 726–730.

43 D. W. Dequilettes, S. Koch, S. Burke, R. K. Paranji, A. J. Shropshire, M. E. Ziffer and D. S. Ginger, *ACS Energy Lett.*, 2016, **1**, 438–444.

44 L. Huang, Z. Ge, X. Zhang and Y. Zhu, *J. Mater. Chem. A*, 2021, **9**, 4379–4414.

45 J. S. W. Godding, A. J. Ramadan, Y. H. Lin, K. Schutt, H. J. Snaith and B. Wenger, *Joule*, 2019, **3**, 2716–2731.

46 H. H. Fang, S. Adjokatse, H. Wei, J. Yang, G. R. Blake, J. Huang, J. Even and M. A. Loi, *Sci. Adv.*, 2016, **2**, 1–10.

47 P. T. Landsberg, *Recombination in Semiconductors*, Cambridge University Press, 2003.

48 P. Wurfel, *J. Phys. C Solid State Phys.*, 1982, **15**, 3967–3985.

49 W. Van Roosbroeck and W. Shockley, *Phys. Rev.*, 1954, **94**, 1558–1560.

50 T. Tiedje, E. Yablonovitch, G. D. Cody and B. G. Brookd, *2017 IEEE Trans. electron devices*, 1984, **ED**-**31**, 711–716.

51 U. Rau, *Phys. Rev. B - Condens. Matter Mater. Phys.*, 2007, **76**, 1–8.

52 V. Sarritzu, N. Sestu, D. Marongiu, X. Chang, S. Masi, A. Rizzo, S. Colella, F. Quochi, M. Saba, A. Mura and G. Bongiovanni, *Sci. Rep.*, 2017, **7**, 44629.

53 H. Tsai, R. Asadpour, J. C. Blancon, C. C. Stoumpos, O. Durand, J. W. Strzalka, B. Chen, R. Verduzco, P. M. Ajayan, S. Tretiak, J. Even, M. A. Alam, M. G. Kanatzidis, W. Nie and A. D. Mohite, *Science*, 2018, **360**, 67–70.

54 B. Guzelturk, T. Winkler, T. W. J. Van de Goor, M. D. Smith, S. A. Bourelle, S. Feldmann, M. Trigo, S. W. Teitelbaum, H. G. Steinrück, G. A. de la Pena, R. Alonso-Mori, D. Zhu, T. Sato, H. I. Karunadasa, M. F. Toney, F. Deschler and A. M.

Lindenberg, *Nat. Mater.*, 2021, **20**, 618–623.

55 O. Cannelli, N. Colonna, M. Puppin, T. C. Rossi, D. Kinschel, L. M. D. Leroy, J. Löffler, J. M. Budarz, A. M. March, G. Doumy, A. Al Haddad, M. F. Tu, Y. Kumagai, D. Walko, G. Smolentsev, F. Krieg, S. C. Boehme, M. V. Kovalenko, M. Chergui and G. F. Mancini, *J. Am. Chem. Soc.*, 2021, **143**, 9048–9059.

56 T. Komesu, X. Huang, T. R. Paudel, Y. B. Losovyj, X. Zhang, E. F. Schwier, Y. Kojima, M. Zheng, H. Iwasawa, K. Shimada, M. I. Saidaminov, D. Shi, A. L. Abdelhady, O. M. Bakr, S. Dong, E. Y. Tsymbal and P. A. Dowben, *J. Phys. Chem. C*, 2016, **120**, 21710–21715.

57 D. Marongiu, S. Lai, V. Sarritzu, E. Pinna, G. Mula, M. Laura Mercuri, M. Saba, F. Quochi, A. Mura, G. Bongiovanni, M. L. M. L. Mercuri, M. Saba, F. Quochi, A. Mura and G. Bongiovanni, *ACS Appl. Mater. Interfaces*, 2019, **11**, 10021–10027.